

# Surface and Bulk Residual Stress in Ti6Al4V Welded Aerospace Tanks

**G. Bruno**

Institute Laue-Langevin,  
BP 156, F-38042 Grenoble,  
France

**B. D. Dunn**

European Space Agency,  
ESTEC, 2200 AG Noordwijk,  
The Netherlands

*The residual stress (RS) in two curved plates cut from a large welded propellant tank for spacecrafts was investigated nondestructively by neutron and laboratory x-ray diffraction. Each plate had two weld beads symmetric to a central monoblock reinforcement. One plate had received a post-weld heat-treatment. The two nondestructive test techniques successfully determined both the bulk (thickness averaged) and the surface stress state, due to the highly different penetration of these radiations in metals. In the as-welded tank, both neutrons and x-rays show a stress level (both in the axial and hoop directions) higher in the heat affected zone (HAZ) than in the weld pool (300 against 160 MPa). A considerable degree of relaxation annealing was observed by neutron diffraction after the application of the heat treatment. In this case, the hoop stress in the HAZ relaxes from about 300 to about 100 MPa. X-rays also permitted the separate determination of the  $\alpha$  and  $\beta$ -phase stresses and the calculation of the macro-RS. The latter showed the bending deformation resulting from the cut of the plates from the original tank. The average stress measured by x-rays was found to be very similar to the RS obtained by neutron diffraction technique. [DOI: 10.1115/1.1763932]*

## 1 Introduction

The standard on-board spacecraft propellant is Hydrazine ( $N_2H_4$ ). This is stored as a liquid in large propellant tanks and fed to small thrusters motors where it is decomposed from liquid  $N_2H_4$  into gaseous ammonia and nitrogen [1].

The hydrazine propellant tanks are fabricated by forging and machining two hemispheres of Titanium alloy Ti6Al4V. Its composition is given in Table 1. The two hemispheres, which have a shell thickness between 2 and 4 mm and an outer diameter of between 0.5 and 2 m are typically joined (girth weld) together by electron beam or Tungsten Inert Gas (TIG) welding.

One failure mode for such welded tanks is known to result from the severe vibration loads, which occur during the launch phase of a spacecraft. In this case rupture takes place in the vicinity of the weld. Furthermore these tanks are submitted to thermal and mechanical cycles during service. It is, then, important that an accurate value is known of the mechanical stress in the welded region of propellant tanks. This is to ensure safety during storage, launch and operational life of the spacecraft.

The stress level caused by the weight of the tank and of the liquid propellant, as well as that due to its pressure, can be easily calculated [2], but in order to evaluate the total stress field it is necessary to detect residual stress (RS) in the component: this has been evaluated in the present work by means of non-destructive x-ray and neutron diffraction techniques.

Very little literature is available on the current subject. RS in Ti6Al4V has been investigated mainly in substrates for coatings [3–5] and biomaterials [6] and in Ti-SiC composites [7,8]. Some Ti6Al4V components have been investigated [9] but, as reported in a preceding work [10], these nondestructive techniques have not been previously applied to titanium alloy weldments.

The complicated microstructure of Ti6Al4V consists of both  $\alpha$  and  $\beta$  phases in the annealed condition. However, the material that has cooled rapidly from the liquid state can result in a wide variety of microstructures that are dependent on the cooling rate. This results in a formidable task for evaluating residual stresses by

means of either neutron or laboratory x-ray diffraction. The use of synchrotron x-rays presents problems of interpretation of the results, due to coarse grain effects.

The present work attempts to assess nondestructively the stress state across the welded region of spacecraft propellant tank, taking into account surface effects, the microstructure and the presence of the  $\beta$ -phase. The efficacy of the standard heat stress-relieving treatment is also tested. The results are also compared with those obtained from destructive RS measurements made using a standard hole drilling/strain gauge technique and with a simple model for RS distributions in welded plates.

## 2 Samples and Microstructure

Two large plate-like samples have been machined from a full size finished propellant tank. These curved plates were identified as X1, as welded, and as X2, after heat treatment. Their size is approximately  $250 \times 250$  and  $250 \times 400$  mm<sup>2</sup>, respectively, and their thickness is 2 mm. Both have been cut with laser technique from a cylindrical tank 515 mm in diameter. The tank was fabricated by joining three forged cylinders using a single-pass tungsten inert gas (TIG) welding technique. The cylinder in the middle has a monoblock reinforcement ring (total thickness 10 mm) at mid-height. The size and shape of the samples are shown schematically in Fig. 1.

The stress relieved sample was heated up to  $485 \pm 8^\circ C$  and held for 4 hours in a  $10^{-4}$  Torr vacuum. A strip about 30 mm wide was successively cut across the weld on sample X2 (along the whole length), again using the laser technique, in order to perform light microscopy and texture analysis. In both cases the cutting procedure is expected to influence the microstructure and the residual stress (RS) state only within a few hundred microns from the cut edge.

From the metallurgical point of view this alloy can be inserted in the titanium ternary alloys near to the pure titanium corner [11]. It is convenient to approach the problem from the binary point of view: this alloy has two coexistent phases, one called  $\alpha$ , with hcp structure and stacking ratio  $c/a=1.59$  (versus the 'ideal' value 1.63), and one called  $\beta$ , having a bcc crystallographic structure. The latter is stable in pure titanium above  $883^\circ C$ , but in this alloy above  $995$  deg C (called the  $\beta$ -transus temperature). This second

Contributed by the Pressure Vessels and Piping Division for publication in the JOURNAL OF PRESSURE VESSEL TECHNOLOGY. Manuscript received by the PVP Division March 13, 2003; revision received March 26, 2004. Associate Editor: W. L. Cheng.

**Table 1** Composition of the Ti6Al4V propellant tanks under evaluation

Element	C	Fe	N <sub>2</sub>	H <sub>2</sub>	O <sub>2</sub>	Al	V	Ti
%wt	0.013	0.16	0.012	0.006	0.11	6.1	4.1	bal.

phase disappears on cooling and transforms into  $\alpha$ , usually in acicular shape, but there are some elements which stabilize it, like vanadium and molybdenum. Usually those elements allow for the presence of the  $\beta$ -phase at room temperature, even if the  $\beta$ -transus is higher than for pure titanium. The presence of this metastable  $\beta$ -phase is seen to also depend on the cooling rate of the material [12]. In weldments this cooling rate will vary and relates to the heat sinking effect of the surrounding tank material [1].

Some small metallographic specimens cut from the parent material, the heat affected zone (HAZ), and the weld pool, have been observed by optical microscopy. The polished cross sections were chemically etched in a mixture of 70 percent H<sub>2</sub>O+30 percent H<sub>2</sub>SO<sub>4</sub> at 70°C, instead of using the standard Keller's reagent (190 ml H<sub>2</sub>O+5 ml HNO<sub>3</sub>+3 ml HCl+2 ml HF).

The resultant micrographs revealed a series of microstructures which showed a transition from the fine grained parent material to the coarse grained weld pool (Fig. 2).

The heat treatment applied to sample X2 has not affected the microstructure, as the temperatures are much lower than the  $\beta$ -transus. From literature [13], the presence of globular  $\alpha$  inside transformed  $\beta$  grains in the parent material (Fig. 2) is well known. Grains containing needle-like  $\alpha$  structures intermingled with residual  $\beta$  were found in the HAZ and in the weld pool. In the HAZ grains reach a size of around 200  $\mu$ m, containing acicular  $\alpha$  in a  $\beta$  matrix, together with serrated  $\alpha$  of planar shape. In the weld, finally, serrated  $\alpha$  structures, with  $\beta$  volume fraction slightly lower than in the HAZ, and acicular  $\alpha$  are present. The average grain size is around 500  $\mu$ m.

The final microstructure of the alloy depends on the cooling speed after solidification; the  $\alpha$  needles become larger as the cooling rate decreases. In our case cooling occurred in a partial vacuum (i.e., under controlled atmosphere) at an intermediate cooling rate, and this caused the microstructure to consist of an acicular  $\alpha$  (martensitic) structure. This acicular structure is quite fine inside both the HAZ and the weld pool.

### 3 Residual Stress Analysis

**3.1 X-Rays Diffraction.** Measurements were made at the X-Ray facility of the Hahn-Meitner Institute, Berlin, Germany, using Cu radiation and a 7 axes diffractometer, equipped with a position sensitive detector (PSD). A thin copper foil was placed in

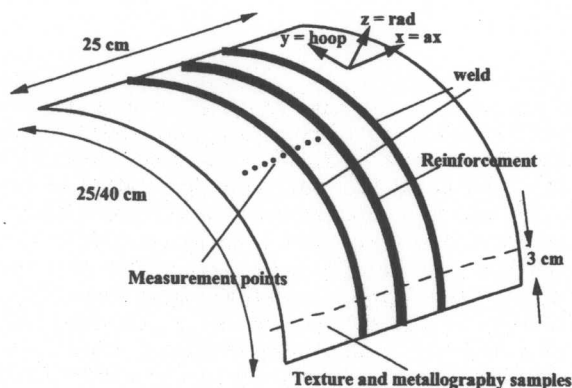


**Fig. 1** Sketch of the sample shape and sizes. Measurement points and the cut made to extract smaller samples are also indicated

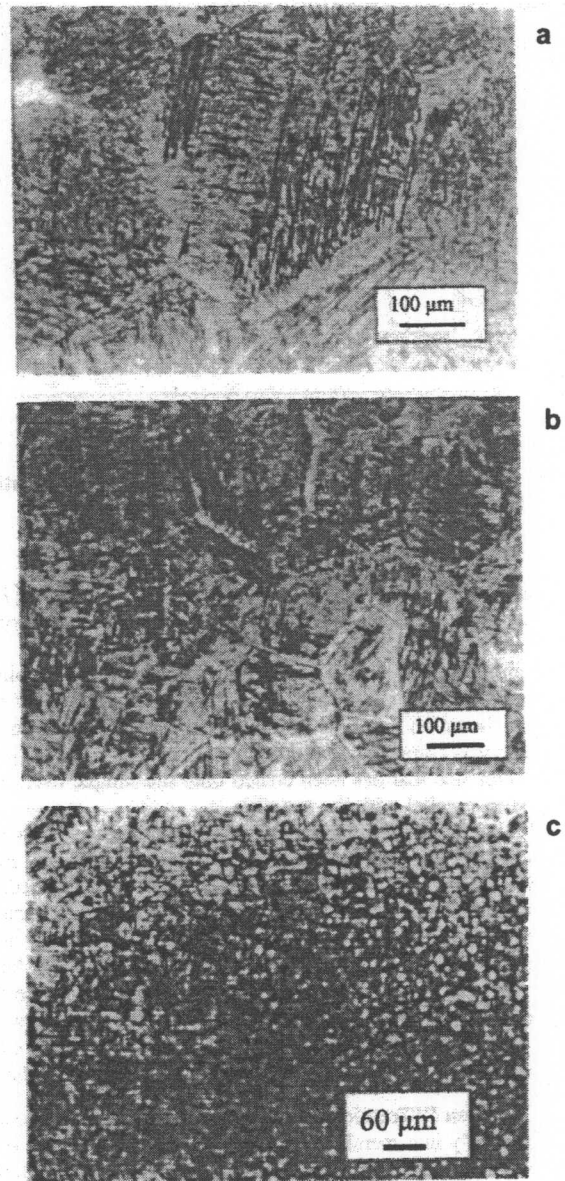


**Fig. 2** Etched cross sections reveal local microstructure variations: (a) the weld pool consists of very large grains, mainly  $\beta$ -phase that has transformed to acicular martensite; (b) the HAZ has the same microstructure, with an intermediate grain size, whereas (c) the parent metal is a mixed structure of globular and small equiaxed  $\alpha$  and  $\beta$  fine grains.

front of the PSD to suppress Ti fluorescence as much as possible [14]. However, the absorption coefficient for Cu radiation in  $\alpha$ - and  $\beta$ -titanium is very high, and sometimes the large background did not permit recognition of the investigated peak. Asymmetric values of  $\psi$  angles were selected while using the  $\sin^2 \psi$  technique [15]. A special sample holder was built to fit the large sample into the diffractometer circle. The so-called  $\psi$ -mode was used, in which the sample is tilted at several angles  $\psi$ , in a direction perpendicular to the scattering plane [16]. A limited angular  $\psi$  range could be accessed, going from  $-50$  to  $60$  deg for both phases. Nine to thirteen  $\psi$  angles and two  $\varphi$  angles were usually investigated, and the same reflections for both samples were exploited, namely the (21 $\bar{3}$ 3) for the  $\alpha$  phase, at  $2\theta \cong 141$  deg, and the (411) for the  $\beta$  phase at  $2\theta \cong 162.5$  deg. Both of these reflections are well separated from all others, and they lie at the highest possible

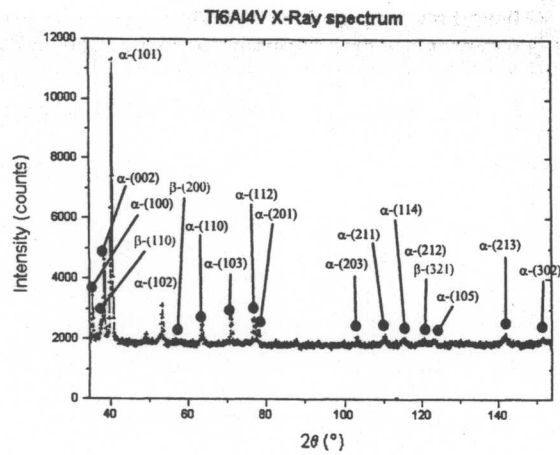


Fig. 3 X-Ray diffraction spectrum obtained with Cu radiation and PSD in the parent material of sample X1 (as-welded)

angle range, thus allowing the best sensitivity and resolution [17]. An entire x-ray spectrum is shown in Fig. 3, containing the angular range  $2\theta \in [35, 153]^\circ$ .

Measurements were performed in each sample at 8 to 10 points, which traverse the weld path, and on a line in the middle of the sample as shown on Fig. 1. In order to avoid effects of the convex shape, data was compared directly with measurements from a gold powder reference that has been coated onto the sample itself and measured in parallel with the samples.

Oscillations of  $\omega$  ( $\pm 3$  deg) were made at each measuring point. In the points of the weld (where the grain size can reach  $500 \mu\text{m}$ ) oscillations along  $y$  (hoop direction) ( $\pm 1$  mm) have been used, in order to calculate an average stress value based on a large number of grains. This was also achieved by selecting a large ( $3.3$  mm diameter) collimator. A further experimental technique has been used to overcome the problem of coarse grain structure inside the weld: some more points on a line along the weld were added (1 for the X2 sample, 3 for the X1, all at a distance of  $3$  mm each other) in order to obtain an average for the  $d$  versus  $\sin^2 \psi$  data.

**3.2 Neutron Diffraction (ND).** As laboratory X-rays do not penetrate deeply into metals (only up to  $10\text{--}20 \mu\text{m}$  from the very surface), neutron diffraction measurements were performed on the  $\alpha$ -phase of both samples in order to verify the bulk macro-stress behavior, averaged over the whole thickness.

Measurements have been carried out with the BER II reactor at the HMI Berlin, using the E3 diffractometer on the T2 (thermal neutrons) line.

The Cu (220) monochromator, i.e., a wavelength of  $1.3822(1)$  Å, has been used. The diffractometer was equipped with a "banana" position sensitive detector (PSD), filled with  $\text{BF}_3$  gas, whose angular  $2\theta$  width is  $80$  deg. The high incoherent neutron cross section of vanadium and titanium, as well as the negative coherent neutron scattering length of titanium, give rise to a large background radiation and to a tiny signal to noise ratio. In those conditions the  $\beta$ -phase was completely undetectable.

A primary collimation window of  $2 \times 2 \text{ mm}^2$  was used, leaving the secondary beam open while looking at peaks in the  $2\theta = 90$  deg region. This ensures an isotropic definition of the gauge volume for each sample orientation [18]. A typical spectrum around  $2\theta = 90^\circ$  is shown in Fig. 4. It can be seen that the  $(21\bar{3}0)$  peak has a very small intensity, and only the other two, namely  $(21\bar{3}1)$  and  $(20\bar{2}3)$ , could be used for RS analysis. Only four points (corresponding to some of those measured with X-rays) in each sample were investigated, due to the long counting times needed (5 hours per point). The axial, radial and hoop directions have been supposed to be the principal ones, so the samples were only measured with the scattering vector  $\mathbf{q}$  lying along those directions.

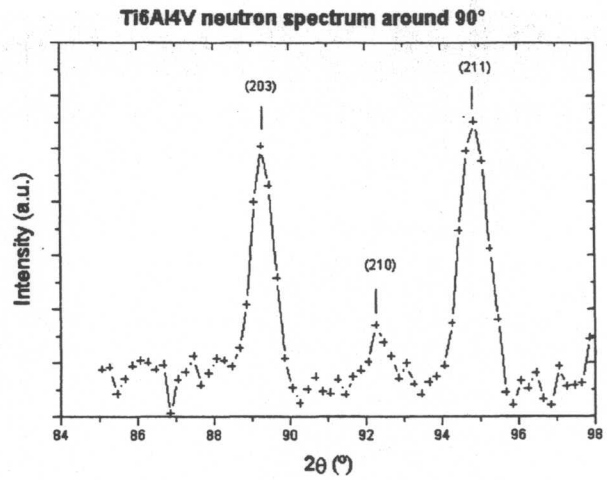


Fig. 4 Typical neutron diffraction spectrum around  $2\theta = 90$  deg. (210) peak results in low intensity and thus was not used for RS analysis. The spectrum was taken in the parent material of sample X1.

The vector  $\mathbf{q} = \mathbf{k} - \mathbf{k}_0$  is the difference between the scattered and incident wave vectors, lying along the respective beam directions and having modulus  $2\pi/\lambda$ , where  $\lambda$  is the wavelength.

**3.3 Hole Drilling.** In a parallel study the RS was destructively evaluated on samples from the same welded pressure vessel. The ASTM standards were followed [19]. Two special three-element strain gauge rosettes were attached to the tank surface, one above the HAZ and the other above the weld bead. In this case the weld bead has been ground flat prior to strain-gauge attachment. The three gauge grids were wired and electrically connected to a static strain indicator. A hole was then drilled into the center of each rosette using small insertion increments. The introduction of a hole relaxes the internal stresses at each location, causing the local surface strains to change correspondingly. The relaxed strains are recorded, and by using special charts [20] they are converted into values of RS.

**3.4 Modeling.** The theoretical analysis of the RS profiles in welds is beyond the scope of this paper. Therefore, neutron and x-ray data were analyzed using a very simple model from Masubuchi and Martin [21,22], where the longitudinal stress, in our case the  $y$ -direction, is modeled as (see co-ordinate definition in Fig. 1)

$$\sigma_y = \sigma_m \cdot \left[ 1 - \left( \frac{x}{b} \right)^2 \right] \cdot e^{-1/2(x/b)^2} \quad (1)$$

In Eq. (1)  $\sigma_m$  is the peak stress and  $b$  is the weld width. As stated in [22], the function  $\sigma_y(x)$  satisfies stress and moment balance, because  $\int \sigma_y(x) \cdot dx = 0$  and the integral of odd functions is zero. There is no analytical model for the transversal stress  $\sigma_x(x)$ , because it doesn't have to satisfy any analytical (balance) condition (along the scan line used) and usually Gaussian profiles (possibly with a flat plateau) are guessed [23]. Although this is a very simplified approach, one must note that more sophisticated analytical models do use the same basis. For example, in [24] the temperature distribution is modelled by a Gaussian function (solution of the Fourier equation in the plate geometry). This brings to a RS profile, which is essentially a sum of exponential functions, multiplied by sine and cosine functions. On the other hand, under realistic conditions, even more simplified approach can be found in literature [25]. With the amount of the present data it was not possible to proceed to a deep theoretical study.

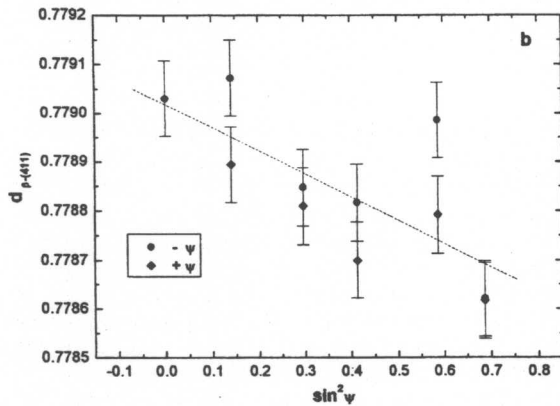
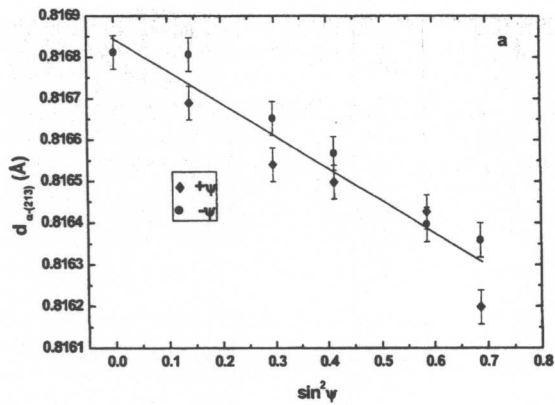


Fig. 5 Examples of  $d$  versus  $\sin^2 \psi$  curves (fitted with straight lines) for  $\alpha$  (a) and  $\beta$ -phase (b) in X1 sample. Both are taken for  $\varphi=90^\circ$ , transversal (axial or  $x$  direction). Positive and negative  $\psi$  values are displayed with different marks.

## 4 Results

**4.1 X-Ray Diffraction.** No remarkable degree of texture could be detected (as reported elsewhere [26]) in either sample X1 or X2, except for some poles in the weld pool. The intensity of these poles suggests that the coarse grain structure can cause such inhomogeneities in an otherwise homogeneous pole distribution. This result is still somewhat unexpected, since at least the forming and drawing processes, used to fabricate the tanks hemispheres, should be supposed to cause surface rolling texture, in the working direction. However, it must be borne in mind that the piece-parts of the tank had been fully annealed prior to welding, and such a heat treatment has probably relaxed both their texture and manufacture stresses.

For sample X1 two examples of  $\alpha$  and  $\beta$ -phase  $d$  versus  $\sin^2 \psi$  curves are shown in Figs. 5(a) and (b) for a point in the parent material.

Within the experimental error one can see that neither texture (true oscillations) nor  $\psi$ -splitting (i.e., no shear stresses) are present. This behavior is identical for all measurement points those except in the weld. For sample X2,  $d$  versus  $\sin^2 \psi$  curves for the  $\alpha$ -phase presented similar characteristics to those in Fig. 5. The weld pool data is again rather scattered (this adds an error of less than 8 percent to stresses), while in the parent material a linear fit is an excellent approximation.

This confirms that the coarse grain effect is quite visible, but true texture cannot be detected. Also in the case of sample X2, the sum of  $d$  versus  $\sin^2 \psi$  data coming from different points of the weld, lying at the same longitudinal ( $y$ ) co-ordinate, has been done.

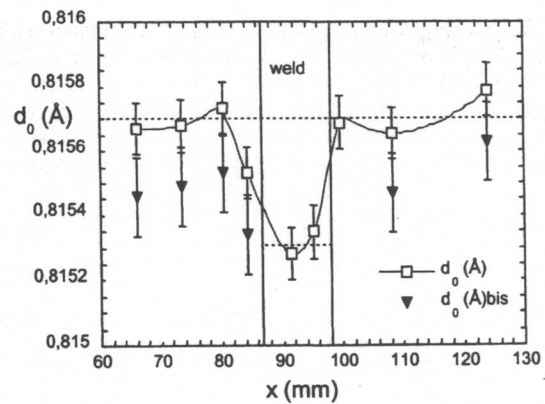


Fig. 6 The  $d_0$  profile across one of the welds for the  $\alpha$ -phase of sample X1, as measured in two successive runs at HMI, X-ray facility

The behavior of the peak integrated intensity, as a function of  $\sin^2 \psi$  is very similar for points in the weld and in the HAZ, and is far smoother for points in the parent material. In the latter region most of the intensities lie in a narrow range, while some  $\psi$  values have larger intensity. The behavior is different in the weld pool and the HAZ: some  $\psi$  angles have exceptionally large intensity and small peak width, while some of them have low intensity and/or large peak width. This is caused by the poor statistics that is obtained when only few grains contribute to the scattered signal. In other words, when the material is not truly polycrystalline, strange peak shapes and odd intensities can be observed, due to non-uniform grain orientation distribution.

The analysis of the  $d$  versus  $\sin^2 \psi$  plots gives us the stresses in the longitudinal and transversal directions from the slopes of the straight lines and the  $d_0$  (unstrained interplanar distance) [15], provided we assume that  $\sigma_z=0$  in the very superficial layer. This hypothesis is justified in absence of surface treatments. The  $\alpha$ -phase  $d_0$  profile is shown in Fig. 6. In this figure the results of successive measurements are recorded. Only a systematic shift due for instance to different alignment conditions is visible. This reflects the reproducibility of the  $d_0$  distribution. The difference of the average unstrained lattice parameter  $d_0(213)$  between the weld region and the base material has been found to be  $4 \cdot 10^{-4}$  Å. Also this difference is extremely reproducible. Both phases have been investigated and the behavior of the stresses  $\sigma_{ax}$  and  $\sigma_{hoop}$  (transversal and longitudinal to the weld respectively,) for the  $\alpha$ - and  $\beta$ -phases is shown in Fig. 7(a, b). In both figures the macro-RS is also shown. It is calculated using Eq. (2) below.

Errors on stresses are calculated by simple error propagation formulas [27], starting from the statistical error on peak position determination.

The hypothesis of vanishing shear stress  $\sigma_{xy}$  was done, so only two  $\varphi$  angles have been used. This hypothesis is indirectly supported (equilibrium conditions) by the absence of  $\psi$ -splitting in the  $d$  versus  $\sin^2 \psi$  curves, which behave fairly as straight lines, implying that  $\sigma_{zy}=\sigma_{xz}=0$ .

For the  $\alpha$ -phase stress evaluation the following elastic constants (EC) have been used:

$$E_{213}=109.9 \text{ MPa} \quad \nu_{213}=0.305$$

They have been calculated with a Kröner model [28]. For the  $\beta$ -phase  $d$  versus  $\sin^2 \psi$  data are more scattered. This is due to low intensity (and sometimes absence) of the (411) peak. Thus, the number of useful  $\psi$  values, which was sometimes 5 or 6, was somewhat reduced. EC used for stress calculation were

$$E_{\beta}=120 \text{ MPa} \quad \nu_{\beta}=0.33$$

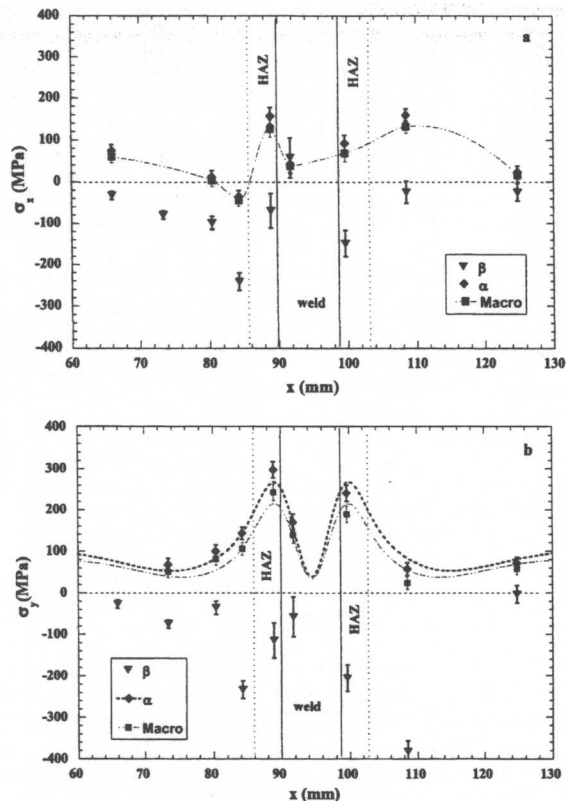


**Fig. 7** Transversal (a) and longitudinal (b) ( $x$  and  $y$ , respectively) stresses for  $\alpha$  and  $\beta$ -phases as measured in sample X1, together with the macro-RS, as calculated from Eq. (2). In the second case the dashed line is a model curve to data, while in the (a) lines are just guides for the eye.

They refer to an alloy Ti-6Al-2Sn-2Zr-2Mo-2Cr+Si (Ti-6-22-22S) [29], in which  $\beta$ -phase is present with higher volume fraction, and are macroscopic values. No microscopic EC are available in literature, but the 411 reflection is essentially elastically isotropic in bcc lattices [30], so macroscopic EC can be reasonably used. For the  $\alpha$ -phase, stresses are always tensile across the weld, reaching up to 300 MPa in the HAZ/weld pool. As it will be seen later, they show behavior very similar to that of neutron measurements. An increase from the parent material to the HAZ and the weld takes place, and the maximum lies always in the HAZ or at its border with the weld.

The joint  $\alpha+\beta$  stress, i.e., the so-called macroscopic stress (M-RS) [31], was evaluated by the formula

$$\sigma_M = f_\alpha \sigma_\alpha + f_\beta \sigma_\beta \quad (2)$$

where  $f_\alpha$  and  $f_\beta$  are the volume fractions of the two phases and  $\sigma_\alpha$  and  $\sigma_\beta$  are the phase-specific total stresses, as evaluated directly by the diffraction data analysis. The volume fraction of  $\beta$ -phase is hard to evaluate exactly, since it is an intragranular phase. A contrast image analysis is difficult and an X-ray fluorescence analysis should be carried out, since a chemical separation is not possible. Furthermore  $f_\beta$  varies slightly as a function of the position  $x$  transverse-to-weld. However, values of  $f_\alpha=0.84$  and  $f_\beta=0.06$  have been reasonably assumed, as in this kind of alloy the  $\beta$ -phase will not exceed 10 percent volume fraction, at room temperature. In Fig. 7 it can be seen that macro stresses are basically the same as the  $\alpha$ -phase stresses. In Fig. 8 the behavior of the transversal and longitudinal stresses for the  $\alpha$ -phase of the sample X2 are displayed. Macro-stress values were used to model the RS profiles of both samples. The oscillations in stress and  $d$  versus  $\sin^2 \psi$  data suggest the presence of (intra and intergranular) micro stresses, due to the stress interaction between the two

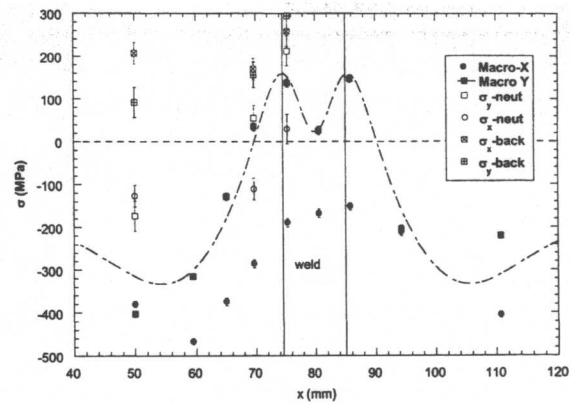


**Fig. 8** Stresses for  $\alpha$ -phase of X2 sample. High compressive values are reached far from weld on the upper (front, convex) side. The stresses on the neutral axis are evaluated as the arithmetic average of the front and back values. Errors are shown only for the “neutral axis” values, but have the same order of magnitude for all points. The fitting curve (Masubuchi function) is also shown thick-dashed.

phases. The data analysis and experimental procedures adopted in this work are best suited to the calculation of macro-stress and the phase-specific total stress, more than for the analysis of micro [31] and intergranular stresses.

Measurements on this sample have been made for  $\varphi=0$  deg and  $90^\circ$  (hypothesis of shear stresses being zero). A smaller difference between the averages of the unstrained lattice parameter inside and outside the weld, than in the X1 sample, has been observed (about  $2.5 \times 10^{-4}$  Å). Both hoop  $\sigma_y$ , and axial  $\sigma_x$  stress profiles are shifted towards negative values and reach  $-400$  MPa in points far from the weld, which are supposed to be unloaded by the welding process. Moreover, both profiles are somewhat stretched: the range of variation of  $\sigma_x$  in sample X1 is about 200 MPa, while it reaches almost 300 MPa in sample X2, although the profile shape in Figs. 7(a) and 8 is quite similar. This odd behavior, which mismatched with neutron diffraction results (discussed later), instigated further investigation. Measurements were next made on the other side of the sample (concave side). They clearly show a bending effect. In fact, on the back side, tensile stress values could be found. The average over the thickness is in good agreement with neutron results, as we will see later. The latter are to be compared with the “neutral axis” values, evaluated as an arithmetic average between front and back values and shown in Fig. 8.

From the analysis of Figs. 7 and 8, a slight asymmetry of the stress profiles can be observed, and the center of gravity seems to be shifted away from the weld center. This can be explained by considering that the central region of the sample (larger  $x$  values) possesses a reinforcement, which strengthens this part and gives rise to different stress levels. This asymmetry was not taken into account in the modeling calculations (see Figs. 7(b) and 8), to avoid the introduction of too many degrees of freedom.

In sample X2 the  $\beta$ -phase stresses have behavior very similar to that of sample X1, with the important difference that asymptotic values are  $-350$  MPa for sample X2, whereas they reach only  $-50$  MPa for X1. However, they were measured only on the front face. This is the reason why in Fig. 8 the M-RS in hoop direction, and not the stress on the neutral axis, was modeled.

The excursion between the weld center and the parent material is also much bigger. This follows the same behavior of the  $\alpha$ -phase stresses.  $\beta$ -phase stresses are shown in Fig. 9.

**4.2 Neutron Diffraction.** In neutron diffraction measurements the principal axes were supposed to lie along the geometrical ones and the hypothesis of plane stress condition over the whole sample was assumed. Both the sample geometry and the

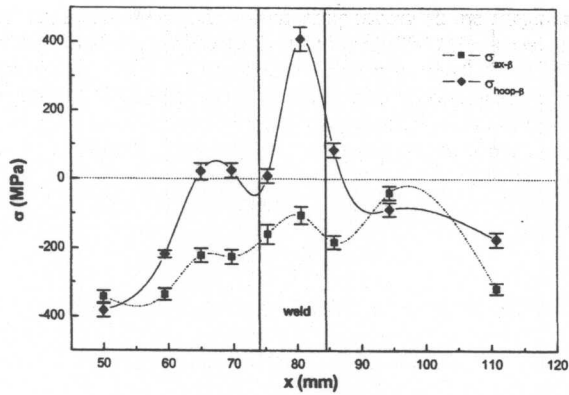


Fig. 9 Stresses (longitudinal and transversal) for the  $\beta$ -phase of the front face of sample X2. As in the  $\alpha$ -phase large negative stresses are present far from weld.

experimental procedure support this hypothesis: neutrons were detected from the complete sample thickness, as no secondary slit was used. In this case (two-dimensional formula) Hooke's law becomes

$$\sigma_{x,y} = \left( \frac{E}{1-\nu^2} \right)_{hkl} \cdot (\epsilon_{x,y} + \nu_{hkl} \epsilon_{y,x}) \quad (3)$$

where  $x, y, z$  are the principal directions and  $E, \nu$  the  $(hkl)$  plane-specific elastic constants. Eq. (3) is valid for  $x$  and  $y$ .

Results on sample X1 (Fig. 11) show a tensile stress state along the investigated region of the sample, both for  $\sigma_{ax}$  and for  $\sigma_{hoop}$ . The radial stress  $\sigma_z$  was evaluated using three-dimensional formula. It is essentially a check on the plane stress hypothesis, and in fact its values vanish within the experimental error, as expected. It must be remarked that the  $d_0$  value was calculated from the plane stress condition and the result is in good qualitative agreement with X-rays. A different average value in the HAZ and the weld pool from the parent material was found, and the difference is around  $4 \cdot 10^{-4} \text{ \AA}$ , the same as in Fig. 6 (X-rays).

In Fig. 11(a, b) stress behavior for the  $(21\bar{3}1)$  and  $(20\bar{2}3)$  peaks is shown for the sample X1, where the elastic constants (EC)

$$E_{211} = 110.6 \text{ GPa} \quad \nu_{211} = 0.293$$

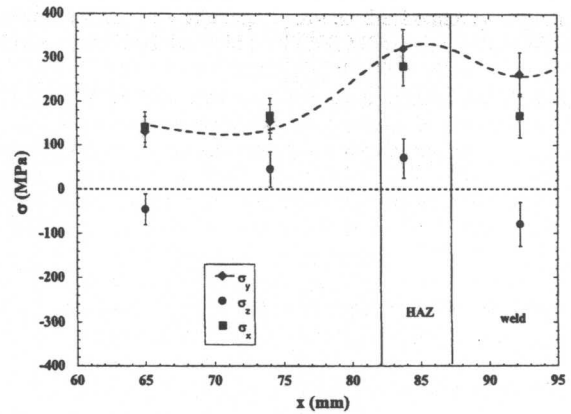
$$E_{203} = 113.0 \text{ GPa} \quad \nu_{203} = 0.283$$

have been used, again according to the Kröner model [28,32], although some discrepancy with experimental data has been found in literature [33,34]. Analogous results for the X2 sample are shown in Fig. 10(a, b) (having used the same EC).

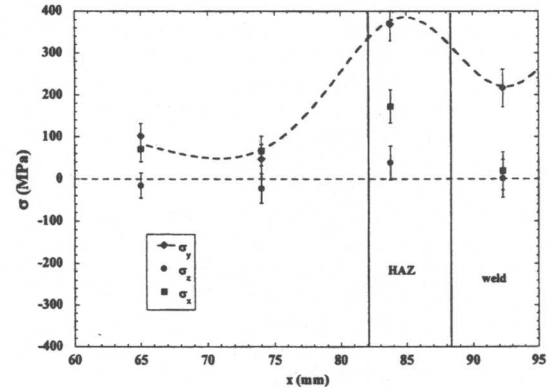
From both Figs. 11 and 10 the following conclusions can be drawn:

- $\sigma_z \approx 0$  everywhere, thus confirming the plane stress hypothesis
- stress values are always reduced in sample X2 with respect to sample X1. In particular in the HAZ they are reduced from about 360 MPa to less than 200 MPa, and in the far field they go from about 100 MPa tensile to slightly compressive values.

**4.3 Destructive Hole-Drilling.** Because of the positioning of the strain gauges, the hole-drilling technique only gave an average of the in-plane stresses. The values of RS for the as-welded tank (no annealing) in the HAZ and in the weld pool were found to be 135 and 95 MPa, respectively. They confirm the trend shown by both x-rays and neutrons: the HAZ is most stressed. The accuracy of this method is considered to be within  $\pm 10$  percent. The method is used as a quality control tool and applied to the testing of samples welded in-line to flight tanks.



(a)



(b)

Fig. 10 Stresses for sample X1 evaluated using neutron diffraction on the  $(203)$  and  $(211)$  peak, (a) and (b), respectively. The fitting curve for  $\sigma_y$  is also shown.

**4.4 Modeling.** All the profiles shown in Figs. 7, 8, 10, and 11 show the influence of the so-called "transformation stresses" [23,35], i.e., have a dip in the weld pool, while a simple Masubuchi-Martin function, Eq. (1), should look bell-like. To model this kind of extra-term a simple parabolic term could be sufficient (since transformation stresses are inherently limited to the weld pool and the HAZ). However, a double Gaussian contribution was preferred in order to fulfil the stress and moment balance conditions:

$$\sigma_y = \sigma_0 + \sigma_w \cdot \left[ 1 - \left( \frac{x}{b} \right)^2 \right] \cdot e^{-1/2(x/b)^2} - \sigma_t \cdot \left[ 1 - \left( \frac{x}{c} \right)^2 \right] \cdot e^{-1/2(x/c)^2} \quad (4)$$

where  $\sigma_w$  is the welding stress,  $\sigma_t$  is the transformation stress,  $b$  is the width of the strain affected zone (SAZ), and  $c$  the width of the region of the weld pool subjected to phase transformation. The constant term  $\sigma_0$  had to be included to take into account the permanent bending effect due to the sample cut (see above and the discussion section).

The fit of the experimental data showed that the SAZ extends to  $b = 12 \pm 2$  mm while the transformed zone extends for  $c = 6 \pm 2$  mm. From the micrographs, the width of the weld pool is about 8 mm. The RS peak values for  $\sigma_w$  and  $\sigma_t$  are very similar in all samples. They are reported in Table 2 for neutron and x-ray data. One must note that the positions of neutron and X-ray diffraction measurements are not the same in both samples (see Figs. 7 and 10, for example). Therefore, an interpolation of the X-ray data on the neutral axis (Fig. 8), using the model outlined here and

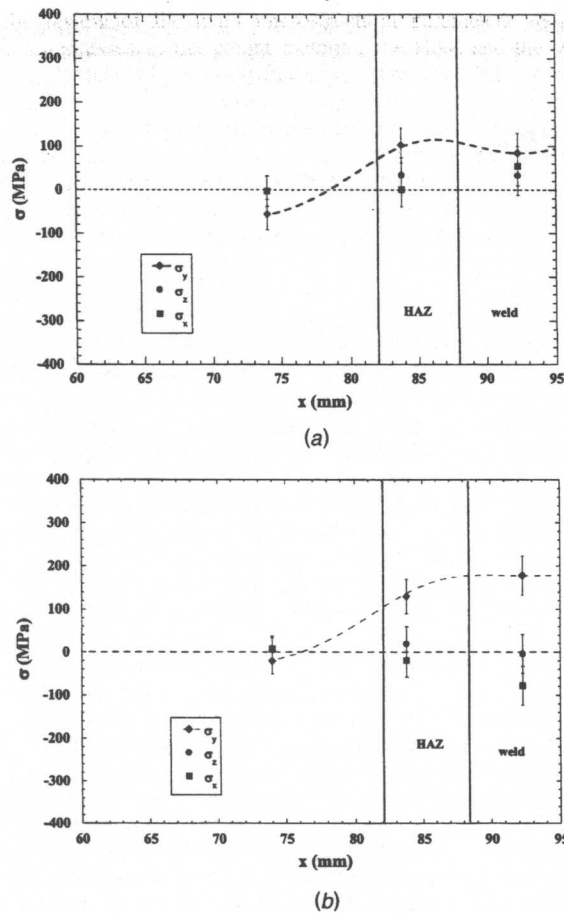


Fig. 11 Stresses for sample X1 evaluated using neutron diffraction on the (203) and (211) peak, (a) and (b), respectively. The fitting line with the Masubuchi-Martin function is also shown.

in section 3.4, was done to extract the (average) X-ray data reported in Table 2. The latter do not correspond to the values shown in Fig. 8.

## 5 Discussion

The RS values obtained from the as-welded (non-heat treated) sample X1 are very similar when calculated from either the neutron diffraction results or the X-ray data. Table 2 gives an over-

view of the main microstructural parameters and the residual stresses in the parent material, the HAZ and the weld pool, as obtained by neutron and x-ray diffraction, from deep hole drilling technique (where strain gauges were used to measure strains) and from the modeling procedure outlined in the previous section. Values of the RS as obtained by neutron diffraction were taken from the average between the (203) and the (211) peaks. A very good agreement can be observed between all techniques. Within the error bars (indicated in Table 2 for the x-component, but similar for the y-direction), neutrons and X-rays give the same response.

For sample X1, the RS profiles are reproduced in both sets of data. In particular, a tensile hoop stress ( $\sigma_y$ ) of about 300 MPa is found in the HAZ. This value is bigger than that in the weld center, as it always happens in boundary regions [36–38], where changes of the microstructure occur. In the parent material (far field), stresses do not relax to zero but reach a constant value of about 80 MPa. X-ray data show a larger difference between longitudinal (hoop) and transversal (axial) stresses than neutron data. However, we must note that neutron data have a coarser step and show a bigger error bar. Neutron diffraction is technically very difficult on this kind of alloy; this is why it was used as a cross-check of x-ray data, to complement surface investigations, as shown in [37].

For the heat-treated sample, X2, the interpretation is more difficult and the need for complementary x-ray (surface) and neutron (bulk) investigations is apparent. While neutron diffraction results do show a stress relaxation after heat treatment, both the X-ray data set and the modelling results (Table 2) show that  $\sigma_y$  attains higher values in the heat-treated sample X2 than in X1. A discrepancy between neutrons and X-rays is also visible for  $\sigma_x$ . This can be explained by several factors: (a) For  $\sigma_y$ , we note that the (203) peak used in ND gives indeed very similar results to X-rays, thus the (211) peak could be in this case suffering from intergranular stress effects [38,9]; (b) The  $\sigma_x$  values in the HAZ are essentially the same, within the error bars indicated in Table 2 (for the transverse component, but similar for the longitudinal one); (c) Looking at Fig. 8, we note that all macro-RS profiles (for both  $\sigma_y$  and  $\sigma_x$ ) are shifted downwards by the permanent bending effect and stretched, probably because of the anticlastic effect [39].

Therefore, the discrepancy between the transverse RS values in sample X2 as obtained by neutron and x-ray diffraction in the PM and the HAZ is only fictitious.

In sample X2, when comparing X-ray with neutron data on the “neutral axis,” a very good agreement can be found. Both techniques show tensile hoop and axial stresses in the HAZ and the weld pool, which revert to compressive stress in the far field. Furthermore, the axial stress profile is flatter than the hoop, and goes almost to zero in both series of data. X-rays show slightly

Table 2 Microstructural parameters and residual stress values for the two samples. X1 = Solution treated and annealed, then welded, X2 = Post-weld heat treated ( $485 \pm 8^\circ\text{C}$  for 4 h). Microhardness measurements were performed at ESTEC, ESA, Noordwijk, The Netherlands; hole-drilling measurements were performed by I.A. Ballinger, Dowty Aerospace, Wolverhampton, UK. Errors on RS are quoted in parentheses for the x-component, but are common to the y-component. Results of the modelling described in the text are also shown.

Sample	Point	Microstructural parameters			Residual Stress (MPa)					
		Micro-hardness (HV)	Grain Size ( $\mu\text{m}$ )	Hole-drilling (in-plane average)	X-rays (average)		Neutrons		Model (Peak Stress)	
					$\sigma_y$	$\sigma_x$	$\sigma_y$	$\sigma_x$	$\sigma_y$	$\sigma_x$
X1	PM	375	10	-	70	80 (10)	80	100 (30)	-	-
	HAZ	375	150	135	300	150 (15)	300	220 (35)	160 (15)	180 (30)
	Weld	375	500	95	160	40 (10)	100	90 (40)	-	-
X2	PM	350	10	-	-80	-110 (10)	-50	20 (30)	-	-
	HAZ	350	150	-	200	30 (15)	120	-10 (35)	280 (45)	100 (30)
	Weld	350	500	-	140	-70 (15)	130	-10 (40)	-	-

higher tensile hoop stress at the boundary region between the HAZ and the weld pool (200 MPa, against the 120 MPa evaluated with neutrons). Obviously, the limited information contained in the neutron data allows a good qualitative, but not quantitative, match. On the other hand neutrons help a lot in recognising that the x-ray measurements on the front face of sample X2 do not represent the whole stress field. This is shown in Fig. 8, in which high compressive values of the longitudinal and transverse stress can be found on the front face. Those values are "neutron balanced" by those on the back face.

As mentioned before, an interpretation of this phenomenon can be given in the following terms: it can be assumed that hoop stresses tend to relax when the propellant tank is cut into small pieces. If the cut piece is short, like sample X1, the hoop stress will vanish at both ends and its value will be smaller in the middle of the sample (i.e., where the measured points lie). If the piece is cut longer, like sample X2 (40 against 25 cm hoop length), then a spring-back effect can cause the onset of flexure stresses, i.e., of a permanent bending effect. Consequently, also the transverse component is influenced, through the anticlastic effect. The stress effectively due to the welding is still retrievable on the neutral axis. This is confirmed on sample X1. Some measurements were done on its back face, in the parent material and the HAZ, but they show this bending effect in a much less visible way, which is the reason why they are not displayed.

The overall stress state is not easy to be fully explained, as it can happen for complex shape components with a complex microstructure. Second and third order stresses play an eminent role in this alloy, as it is confirmed by the somewhat oscillating behavior of the  $\beta$ -phase stresses.

The experimental procedure and the data analysis adopted here allow only their indirect determination. Furthermore, the presence of local shear stresses may also influence the stress state, as the stress ellipsoid could rotate at the weld border, because of the principal stress gradients  $\partial\sigma_{xx}/\partial x$  and the equilibrium relation

$$\frac{\partial\sigma_{xx}}{\partial x} + \frac{\partial\sigma_{xy}}{\partial y} + \frac{\partial\sigma_{xz}}{\partial z} = 0$$

However, as stated above, radial ( $z$ ) shear stresses were not observed, since no  $\psi$ -splitting has been found, and  $x, y$  shear stresses were not revealed in some check measurements where 3  $\varphi$  angles were used (not shown).

## 6 Conclusions

Macro-stresses are accurately determined by means of neutron diffraction. Neutrons show how heat treatment of the propellant tank was very effective in reducing (but not yet eliminating) residual stress. The maximum hoop stress is reduced from about 300 MPa to about 160 MPa. Hoop stresses seem to be everywhere tensile in sample X1 (in the near parent material) and larger in the HAZ than in the weld pool. A three-dimensional analysis also confirms the validity of the hypothesis of plane stress for such a thickness. Neutron measurements also show how hoop stresses tend to revert their sign in the parent material, after the heat treatment. However, they are affected by rather large errors (around 40–50 MPa). X-ray inspections greatly assist in resolving the details of the stress profiles, and evaluating (here for the first time, as a novelty) the  $\beta$ -phase stresses. X-rays show how bending effects can play an important role. In sample X2, large compressive stresses on the upper (front) face have been found (down to 400 MPa), while the back (concave) face is subjected to tensile stresses. Their average, which represents what neutrons 'see,' agrees in fact very well with neutron diffraction investigations. It is thought that a geometrical effect (the larger hoop size of sample X2) brings about this bending effect, which is less visible on the physically smaller sample X1. X-rays also show how both axial and hoop stresses (respectively transversal and longitudinal to the

weld) actually revert their sign in the far field of sample X2. The absence of shear stresses is another by-product of these x-ray investigations.

## Acknowledgment

The authors wish to thank J. Linhart (HMI, Berlin, Germany) and W. Reimers (now at TU-Berlin, Institute for Metal Physics) for the great help in performing experiments and data analysis. Special thanks go to Ian Ballinger (Dowty Aerospace, Wolverhampton, UK) for performing the heat treatment and the hole drilling tests. Financial support by the HMI is kindly acknowledged, in the frame of the EU program "Access to Large Scale Facilities." Finally, F. Fiori and G. Albertini (INFM Unit of Ancona, Italy) gave precious suggestions for data interpretation.

## Nomenclature

- $\sigma_{xy}$  = (shear) component of the stress tensor acting on a face of the elementary cube perpendicular to  $x$  and parallel to  $y$
- $\partial\sigma_{xy}/\partial x$  = its derivative along the direction  $x$
- $\sigma_z$  or  $\sigma_{zz}$  = principal and normal component of stress, respectively
- $(hkl)$  = Miller's notation for the crystallographic indices of a lattice plane
- $(hk\bar{l})$  = Miller's notation for the crystallographic indices of an hexagonal lattice plane, with  $i = -k - h$
- $\lambda$  = wavelength (neutrons and x-rays)
- $d_{hkl}$  = lattice spacing of the  $(hkl)$  plane
- $d_{0(hkl)}$  = reference, unstrained, lattice spacing of the  $(hkl)$  plane
- $2\theta$  = Bragg's scattering angle for diffraction
- $\mathbf{q}$  = scattering vector, in the direction of strain measurements
- $\mathbf{k}, \mathbf{k}_0$  = scattered and incident wave vectors, of modulus  $2\pi/\lambda$
- $E_{hkl}$  = microscopic Young's modulus of the  $(hkl)$  lattice plane
- $\nu_{hkl}$  = microscopic Poisson's ratio of the  $(hkl)$  lattice plane
- $f_\alpha$  = volume fraction of the phase  $\alpha$
- $\psi$  = sample tilting angle with respect to the scattering plane
- $\varphi$  = sample rotation angle around its surface normal

## References

- [1] Dunn, B. D., ed., 1997, *Metallurgical Assessment of Spacecraft Parts, Materials and Processes-II*, Praxis Publishing, Chichester, UK.
- [2] Laroze, S., and Barrau J. J., 1991, *Mecanique des structures*, tome 1, Solides elastiques, plaques et coques, Masson, Paris.
- [3] Scardi, P., Leoni, M., Cappuccio, G., Sessa, V., and Terranova, M. L., 1997, "Residual Stress in Polycrystalline Diamond/Ti-6Al-4V Systems," *Diamond Relat. Mater.*, 6, pp. 807–811.
- [4] Härtling, M., and Fritsch, G., 1996, "Determination of the Residual Stress State in a Natural Titanium Oxide Layer," *Acta Mater.*, 44, pp. 487–492.
- [5] Paturaud, C., Farges, G., Sainte Catherine, M. C., and Machet, J., 1998, "Influence of Particle Energies on the Properties of Magneton Sputtered Tungsten Films," *Sur. Coat. Technol.*, 98, pp. 1257–1261.
- [6] Tsui, Y. C., Doyle, C., and Clyne, T. W., 1998, "Plasma Sprayed Hydroxyapatite Coatings on Titanium Substrates, Part I: Mechanical Propertie and Residual Stress Levels," *Biomaterials*, 19, pp. 2015–2029.
- [7] Choo, H., Rangaswamy, P., and Bourke, M. A. M., 2000, "Internal Strain During Heating of Ti-6Al-4V/SCS-6 Composite," *Scr. Mater.*, 42, pp. 175–181.
- [8] Hanan, J. C., Swift, G. A., Üstündag, E., Beyerlein, I. J., Almer, J. D., Lienert, U., and Haeffner, D. R., 2002, "Microscale Elastic Strain Evolution Following Damage in Ti-SiC Composites," *Metall. Mater. Trans. A*, 33, pp. 3839–3845.
- [9] Evans, A. D., King, A., Pirling, T., Bruno, G., Withers, P. J., and Woodward, C., 2003, "Determination of Residual Stress in Laser Shock Peened Ti-6Al-4V," Ti-2003-10th World Conference on Titanium, Hamburg, Germany, in press.
- [10] Bruno, G., Carradò, A., Dunn, B. D., Fiori, F., Girardin, E., Pirling, T., and Rustichelli, F., 2000, "Neutron Diffraction Measurements for the Determination of Residual Stress in Ti6Al4V Welded Plates," *Mater. Sci. Forum*, 347–349, pp. 684–689.

- [11] Villars, P., Prince, A., and Okamoto, H., eds., *Handbook of Ternary Alloy Phase Diagrams*, ASM International, Materials Park, OH.
- [12] Ivasishin, O. M., Markowsky, P. E., Matviychuk, Yu. V., and Semiatin, S. L., 2003, "Precipitation and Recrystallization Behavior of Beta Titanium Alloys during Continuous Heat Treatment," *Metall. Mater. Trans. A*, **34A**, pp. 147–158.
- [13] *ASM Metals Handbook*, 1993, vols. 2 and 9, Materials Park, OH.
- [14] Bollenrath, F., Fröhlich, W., Hauk, V., and Sesemann, H., 1972, "Röntgenographischen Elastizitätskonstanten von Titan und Ti6Al4V," *Z. Metallkd.*, **63**, pp. 790–801.
- [15] Dölle, H., and Hauk, V., 1976, "Röntgenographische Spannungsermittlung für Eigenspannungssysteme allgemeiner Orientierung," *Härterei Tech. Mitt.*, **31**, pp. 165–168.
- [16] Noyar, I. C., and Cohen, J. B., 1987, *Residual Stress: Measurement by Diffraction and Interpretation*, Springer Verlag, New York.
- [17] Cullity, B. D., 1978, *Elements of X-Ray Diffraction*, Addison and Wesley, Reading, MA, pp. 447–478.
- [18] Webster, P. J., 1992, "Spatial Resolution and Strain Scanning," in *Measurement of Residual and Applied Stress Using Neutron Diffraction*, M. T. Hutchings and A. D. Krawitz, eds., Kluwer Academics, Dordrecht, The Netherlands.
- [19] *ASM Metals Handbook*, 2000, "Mechanical Testing & Evaluation," **8**, Materials Park, OH.
- [20] ASTM Standard E835-94A, 1994, "Standard Test Method for Determining Residual Stresses by the Hole-Drilling Strain Gauge Method," ASTM, West Conshohocken, PA.
- [21] Masubuchi, K., and Martin, D. C., 1961, "Investigation of Residual Stresses by Use of Hydrogen Cracking," *Welding Journal (Miami, FL, U. S.)*, **40**, research supplement, pp. 553s–563s.
- [22] Masubuchi, K., 1980, *Analysis of Welded Structures*, Pergamon Press, Oxford, Chap. 6 and 12.
- [23] Wohlfahrt, H., 1976, "Schweißbeigenspannungen," *HTM Beiheft*, **31**, pp. 56–71.
- [24] Umemoto, T., and Furuya, S., 1989, "A Simplified Approach to Assess Weld Residual Stress Distribution Through Pipe Wall," *Nucl. Eng. Des.*, **111**, pp. 159–171.
- [25] Basavaraju, C., 2000, "Simplified Analysis of Shrinkage in Pipe to Pipe Butt Welds," *Nucl. Eng. Des.*, **197**, pp. 239–247.
- [26] Bruno, G., and Dunn, B. D., 2004, "Texture of  $\alpha$  and  $\beta$  Phases in Ti6Al4V Welded Aerospace Tanks," in progress.
- [27] Taylor, J. R., 1982, *An Introduction to Error Analysis: The Study of Uncertainties in Physical Measurements*, University Science Books, New York.
- [28] Behnken, H., and Hauk, V., 1986, "Berechnung der röntgenographischen Elastizitätskonstanten (REK) des Vielkristalls aus Einkristalldaten für beliebige Kristallsymmetrie," *Z. Metallkd.*, **77**, pp. 620–626.
- [29] Kuhlman, G. W., Rohde, K. A., and Chakrabarti, A. K., 1993, in *Titanium '92, Science and Technology*, Proceedings of the 7th World Titanium Conference, F. H., Froes and I. L. Caplan, eds., San Diego, CA, pp. 1371–1378.
- [30] Pang, J. W. L., Holden, T. M., and Mason, T. E., 1999, "Intergranular Stresses in 350WT Steel," *J. Strain Anal.*, **33**, pp. 373–383.
- [31] Pintschovius, L., 1992, in *Measurement of Residual and Applied Stress Using Neutron Diffraction*, M. T. Hutchings and A. D. Krawitz, eds., Kluwer Academics, Dordrecht, pp. 115–130.
- [32] Evenschor, P. D., and Hauk, V., 1972, "Berechnung der röntgenographischen Elastizitätskonstanten aus den Einkristallkoeffizienten hexagonal kristallisierende Metalle," *Z. Metallkd.*, **63**, pp. 798.
- [33] Bruno, G., and Dunn, B. D., 1997, "Precise Measurement of Ti6Al4V  $\alpha$ -(0111) Elastic Constants by Means of Neutron Diffraction," *Meas. Sci. Technol.*, **8**, pp. 1244–1249.
- [34] Butler, B. D., Murray, B. C., Reichel, D. G., and Krawitz, A. D., 1989, "Elastic Constants of Alloys Measured With Neutron Diffraction," *Adv. X-Ray Anal.*, **32**, pp. 389–394.
- [35] Macherrauch, E., and Wohlfahrt, H., 1977, "Die Ursachen des Schweißbeigenspannungszustandes," *Materialprüfung*, **19**, pp. 272–284.
- [36] Nitschke-Pagel, T., and Wohlfahrt, H., 2000, "Residual Stress Relaxation in Welded High Strength Steels Under Different Loading Conditions," *Proceedings ICRS-6 Oxford*, UK, pp. 1495–1502.
- [37] Albertini, G., Bruno, G., Dunn, B. D., Fiori, F., Reimers, W., and Wright, J. S., 1997, "Comparative Neutron and X-Ray Residual Stress Measurements in AA2219 Welded Plate," *Mater. Sci. Eng.*, **A224**, pp. 157–165.
- [38] Bruno, G., 2002, "Relaxation of Residual Stress in As-Welded and Aged AISI 347 Pipe by Means of Time-of-Flight Neutron Diffraction," *Z. Metallkd.*, **93**, pp. 33–41.
- [39] Timoshenko, S., and Woinowsky-Kreiger, S., 1969, *Theory of Plates and Shells*, McGraw and Hill, New York.